Finite Element Analysis Validation for Stitched, Blade-Stiffened Aerospace Structures

Erin Anderson[1], Alana Zahn Cardona[1], and Andrew E. Lovejoy[2]
NASA Langley Research Center, Hampton, VA, 23681, USA

Increased performance and manufacturing rates for aircraft or spacecraft structures may be achieved using stitched and resin infused composite structures. In order to carry out design and analysis of stitched composites, 2-dimensional (2-D) and 3-dimensional (3-D) modeling approaches for stitched and non-stitched carbon fiber vacuum-infused parts were developed. These analysis approaches will be compared with data from previous test specimens tested at the NASA Langley Research Center (LaRC) under tension and bending load conditions. The preliminary results presented herein for the 2-D and 3-D models capture the strain patterns observed in digital image correlation (DIC) data for stitched, blade-stiffened specimens tested in either tension or bending. The analysis method study presented for these specimens is part of a larger analysis development effort planned for stitched composites, with the modeling practices developed here contributing to those that may be applied to a new set of blade-stiffened test specimens that are currently being manufactured for testing as well as the design of a blade stringer pull-off test. These future tests are expected to provide opportunities to validate the developed modeling approaches for predictive purposes, and to provide opportunities for further refinement of the modeling approaches.

I. Introduction

Increased performance and manufacturing rates for aircraft or spacecraft structures may be achieved using stitched and resin infused composite structures. The National Aeronautics and Space Administration (NASA) Hi-rate Composite Aircraft Manufacturing (HiCAM) Project is planning to examine various technologies to increase manufacturing rate for composite commercial transport aircraft structures, including stitched, resin-infused composites. These stitched composite structures are highly unitized, and stitched composite test articles that were tested at NASA Langley Research Center (LaRC) have demonstrated performance benefits.[1-3] These previous test articles were stitched and resin-infused and used the pultruded-rod, stitched, efficient, unitized structure (PRSEUS) concept, where the stitching consists of Vectran$^{\phi}$ thread.[4] Vacuum infusion of these complex, dry preforms offers an opportunity for decreased manufacturing time by reducing the number of steps in final product assembly. Superior strength and damage tolerance properties are also possible, with co-infusion of parts including through-thickness reinforcement resulting in higher failure loads. While the potential advantages offered by composite parts are widely accepted, analysis models of these parts are often performed using simplified approaches for initial sizing and design. As computing costs are reduced and speeds are increased, more detailed analytical models become reasonable investments earlier in the design process to account for design details such as stitching. These modeling approaches need to be validated via test programs before being adopted for use in design during HiCAM and other projects.

In this paper, 2-dimensional (2-D) and 3-dimensional (3-D) finite element modeling approaches are presented for non-stitched and stitched test specimens of a T-cap structure subjected to tension or bending loads. The integral T-cap structure, shown in Fig. 1, is a T-shaped solid laminate where the top of the T is stitched to the skin of a panel, and the body of the T serves as a stiffener. In the referenced investigation, it was introduced for use in a pressurized test article to connect adjacent panels of PRSEUS structure.[1] The T-cap is similar to a blade stiffener and was chosen for model development because test data was available from previous testing performed at LaRC.[5, 6] It is termed the T-

[1] Research Aerospace Engineer, Structural Mechanics and Concepts Branch, Member AIAA.
[2] Senior Research Aerospace Engineer, Structural Mechanics and Concepts Branch, Associate Fellow AIAA.
$^{\phi}$ The mention of a company or product is not an endorsement by the National Aeronautics and Space Administration (NASA).

cap because it replaces the cap portion of the attached structure, such as the PRSEUS panel or a spar web in a wing. The simplified 2-D model was constructed to allow for an easily modifiable model intended for use early in the design process to assess stacking sequence and the presence of stitches. The 3-D model is intended for detailed analysis of a more mature design to predict detailed failure mechanism development. In the paper, ply layers were individually modeled in both models to determine the ply location of failure in each test specimen. The representative T-cap structure that comprises carbon fiber and resin composite plies, with a "noodle" structure consisting of a braided noodle preform co-infused with the T-cap plies, is shown in Fig. 1. The white dashed lines denote the locations and orientations of the stitching thread through the T-cap. The web and skin stacks consist of repeated multi-ply non-crimp fabric stacks, with each stack consisting of a [+45, -45, 0, 90, 0, -45, +45] layup, with percentages of the 0-degree, 45-degree, and 90-degree fibers equal to 44.9%, 42.9%, and 12.2%, respectively.

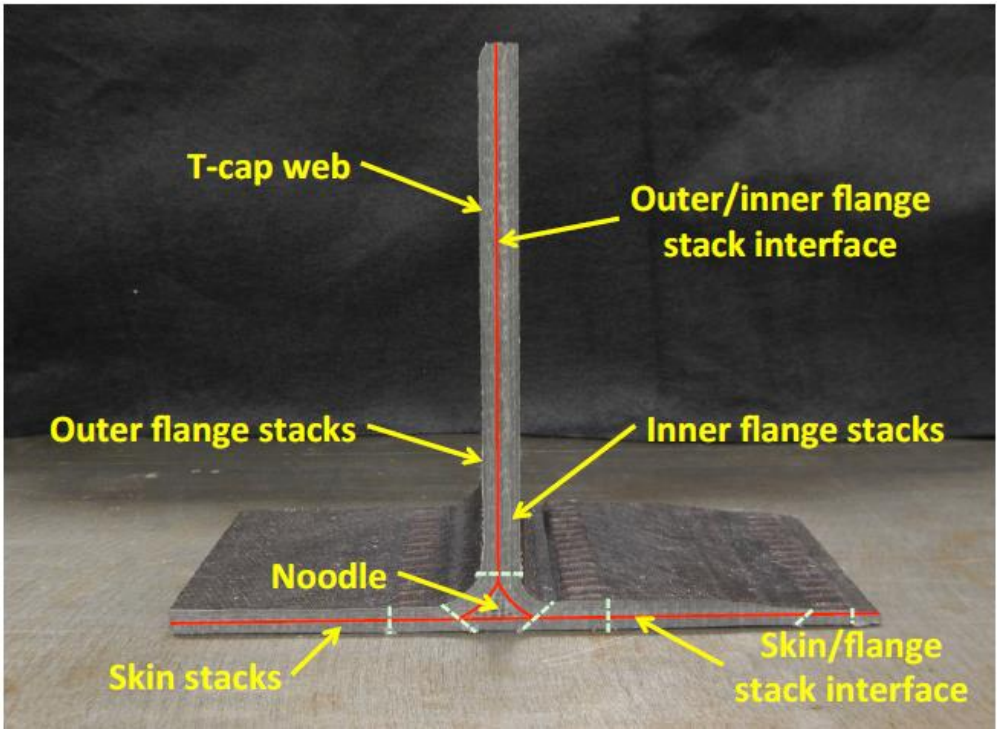

Fig. 1 Integral T-cap used to develop analysis modeling approaches.

The development of 2-D and 3-D modeling approaches for stitched and non-stitched carbon fiber vacuum-infused parts is discussed herein. These modeling and analysis approaches will be compared with data from previous test specimens under tension and bending load conditions. Descriptions of the test setup and finite element models are in Section II. Results from the finite element models are located in Section III. A correlation to test data and a brief discussion of the results are presented in Section IV, and finally the conclusions are presented in Section V.

II. Finite Element Modeling

The test results from previous T-cap tests[5, 6] were used to validate the finite element models that are the subject of this paper. The 2-D and 3-D models were developed for the T-cap cross section shown in Fig. 1. These T-caps were cut from a representative aircraft keel that was fabricated as part of the Environmentally Responsible Aviation (ERA) project for the hybrid-wing-body multi-bay box test article.[7] The T-caps were fabricated using dry non-crimp fabric stacks that were stitched together to form a dry preform, and then resin infused in a vacuum-assisted resin transfer molding (VARTM) process. To form the tested T-caps, three stacks of material were used for the skin, three stacks were used for the outer flange side of the T-cap, and four stacks were used on the inner flange side of the T-cap. The fillet radius at the base of the T-cap web was approximately 0.25 inches on both sides. Each material stack had a cured thickness of 0.052 inches. Cross-sectional dimensions of the T-cap test specimen are shown in Fig. 2, where each color represents a preformed stack of material comprised of the aforementioned standard layup. The depth of each test

specimen was 2.9 inches. The directions of the tension load and the bending load that were individually applied during testing are also shown in the figure. The test articles were installed in one of the two test fixtures shown in Fig. 3; articles were mounted via a bolt and clamp plate on the skin and flange on both sides of the web. Complete details of the test setup and test articles can be found in Ref. 6.

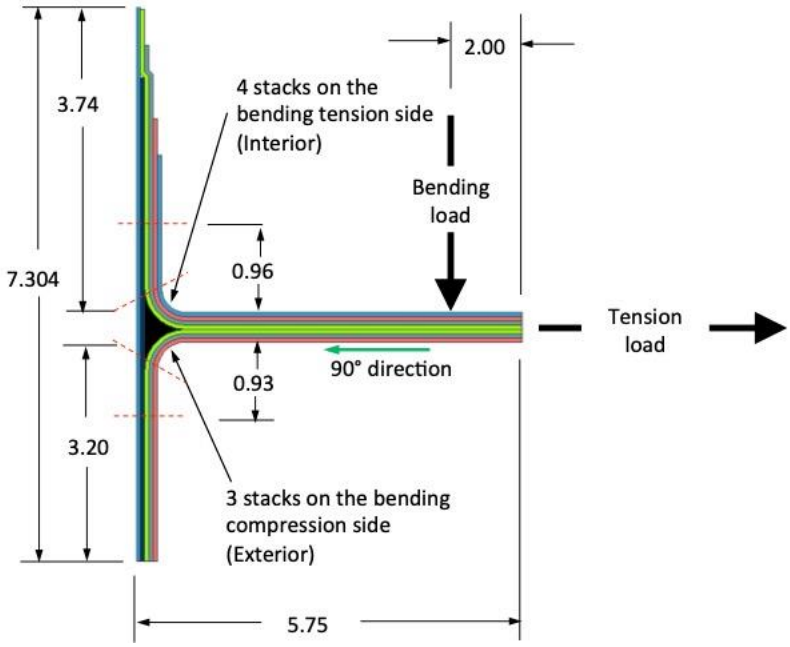

Fig. 2 Integral T-cap dimensions and applied load directions.

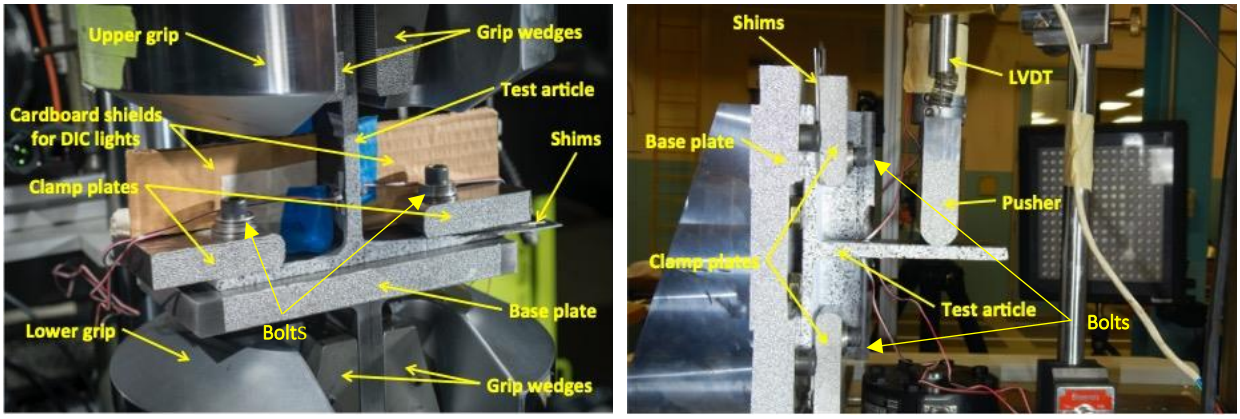

a) Tension test set-up b) Bending test set-up

Fig. 3 Integral T-cap dimensions and applied load directions.

The 2-D model of a cross section taken through the center of a representative test specimen was created in the commercial finite element code Abaqus.[8] The model consisted of 9383 S4R and 5 S3R 2-D 4-noded quadrilateral and 3-noded triangular elements, respectively. Shell elements were selected in lieu of plane strain elements as this method has been shown to produce acceptable results in prior unpublished research. For the stitched model, 2-D connector elements were used to model stitches through the cross section. These elements were assigned Vectran thread material properties in the axial direction, as found in Ref. 4, and provide stiffness through the ply layers. Individual plies were modeled, with one element modeled through the thickness of each ply. Detail of the unstitched model, with elements colored by corresponding ply type, is shown in Fig. 4, with the zero-degree plies in purple, the 45-degree plies in blue, and the 90-degree plies in green. Applied loads and boundary conditions corresponding to test conditions are depicted

in Fig. 5. Ply elements were modeled in greater density closer to the noodle and region of interest at the radius of the web, with elements along the radius having a maximum length of 0.05 in. Elements outside the region of interest were increased to a maximum length of 0.2 in. As each element represented the thickness of a ply, the length of each element in the direction through the thickness was determined by the approximate real-world ply thickness.

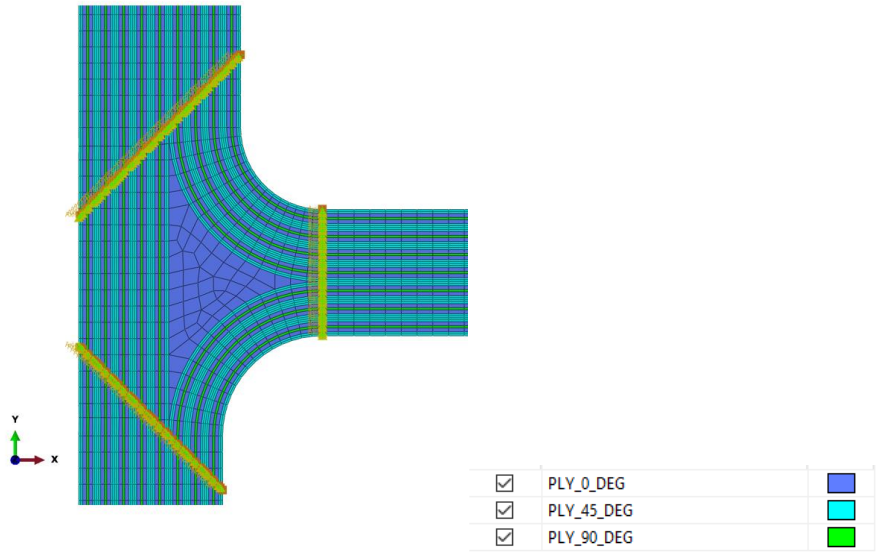

Fig. 4 2-D model colored by material type and with stitches indicated.

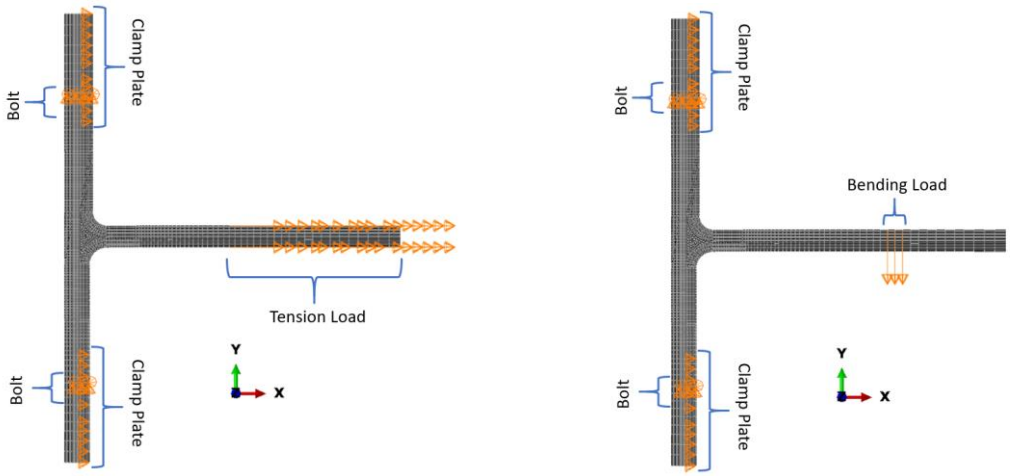

Fig. 5 Boundary conditions on 2-D model for a tension load case (left) and bending load case (right) on a specimen without stitches.

Boundary conditions were applied to the model, including zero-displacement boundary conditions in the global x-direction applied to the surface nodes on the flange plies corresponding to the location of the clamp plates, and zero displacement in the y-direction enforced at nodes corresponding to the locations of the bolts through the skin and flange thickness (see Fig. 3 for clamp detail and bolt locations). All nodes in the 2-D model were given a zero-displacement boundary condition in the z-direction to ensure that the cross section remained planar. This condition is also enforced for both the tension and bending load cases but is excluded from the plots in Fig. 5 for clarity. For the tension load case, an enforced displacement of 0.03 in. was applied to the web at the location of the test fixture grips as a ramp from zero to the final displacement. For the bending load case, a displacement of 0.1 in. was applied to the web at the location of the crosshead pusher bar (labeled LVDT in Fig. 3), also as a ramp. These displacements are consistent with the crosshead displacements at the point of test specimen failure for experimental tension and bending configurations. Material properties were taken from Ref. 10 and the 2-D models were analyzed using an Abaqus static

nonlinear analysis.[9] The corresponding failure loads for the tension and bending cases were recovered by the summation of the reaction forces at the clamp surfaces.

The 3-D models were created with 8-noded or 6-noded reduced-integration continuum shell elements (SC8R or SC6R, respectively) for all of the laminate plies, general purpose linear brick elements (C3D8) for the noodle elements, and 2-noded beam elements (B31) for all stitch elements. The elements close to the web and stitch regions were 0.08 in. by 0.08 in. in the plane of the ply and varied in depth according to the real-world thickness of each ply. Elements toward the outer transverse edges of the skin and flange were 0.12 in. by 0.08 in. in the plane of the ply and varied in depth according to the real-world thickness of each ply. Two 3-D models were developed with stack-based, through-thickness elements, but only one contained the stitch detail. The models, shown in Fig. 6, had one element through the thickness for each stack. The beam elements representing stitches were created from the nodes through the thickness within the skin, flanges, and web. The nodes were chosen at spacing increments representative of actual stitch lengths used in the T-cap specimens. A slice through the skin and flange and a slice through the web is shown in Fig. 7 at the stitch locations. These beams were used to provide extra stiffness at the stitch location and contained the Vectran thread material properties and dimensions previously referenced. The stitch path on the outer surfaces are not modeled, which conservatively assumes that the through-thickness stitch provides strength but does not pull on the surface portions of the stitch seam. This assumption is made because of stitch slack after resin infusion when compared to stitch application on the more expanded dry material.

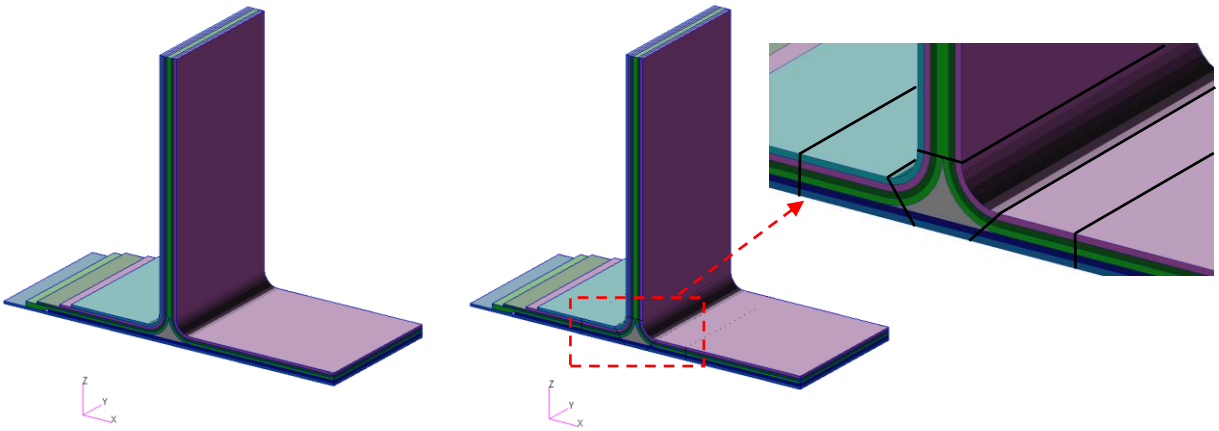

Fig. 6 Stack-based 3-D T-cap models without stitches (left), and with stitches (right).

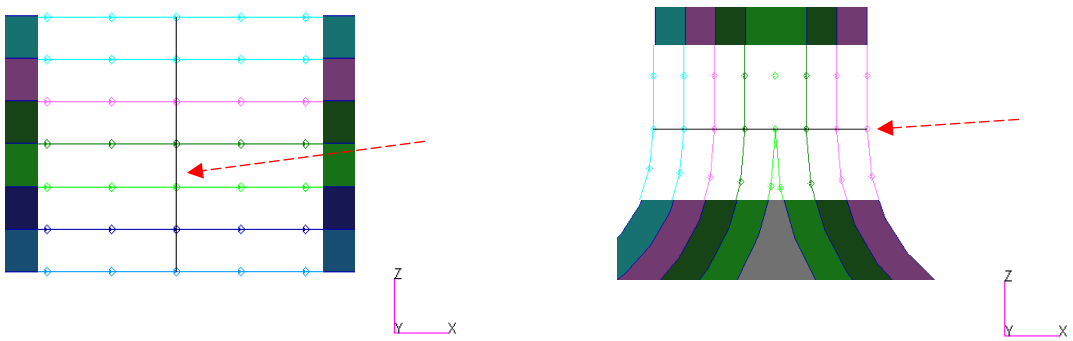

Fig. 7 Stitch locations in the skin flange (left) and the web (right) in the 3-D model. Stitches are shown in black and indicated by the dotted red arrow; adjacent solid elements are shown as colored outlines.

The 3-D models were also run using a nonlinear static analysis with the Abaqus built-in damage mode. After the nonlinear static analyses were fully investigated and compared against the test data, the models were run with progressive failure analysis (PFA) using the Hashin failure criteria and the previously used Abaqus built-in damage model. The Hashin fiber and matrix tensile failure modes were used for the tension analyses, and these tensile failure modes were used along with the Hashin fiber and matrix compressive failure modes for the bending analyses. This failure analysis was completed as part of forward work, and only the pre-failure results are discussed in this paper for

brevity. For each model, boundary conditions were applied at the nodal regions that represented the test stand configurations shown in Fig. 3. The clamped boundary conditions in Fig. 8a are shown in orange along the skin and flange surfaces, including bolt locations through the thickness of the skin and flange. Along the top of the web, either tension or bending boundary conditions, as shown in Figs. 8b and 8c, respectively, were replicated at the nodal regions shown in orange. Displacement control was used to apply the loading, and the corresponding failure load was confirmed by the summation of the reaction forces at the clamp surface.

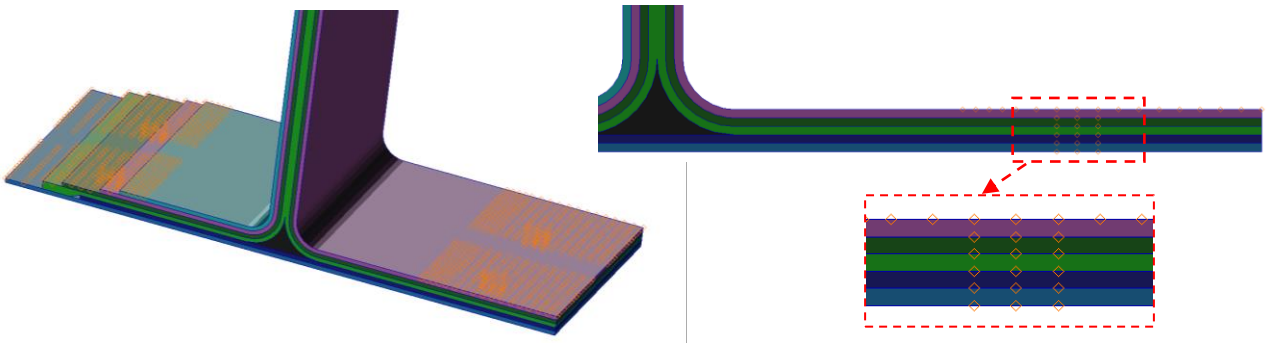

a) Clamp boundary conditions along skin surface (left), and bolt conditions through thickness (right).

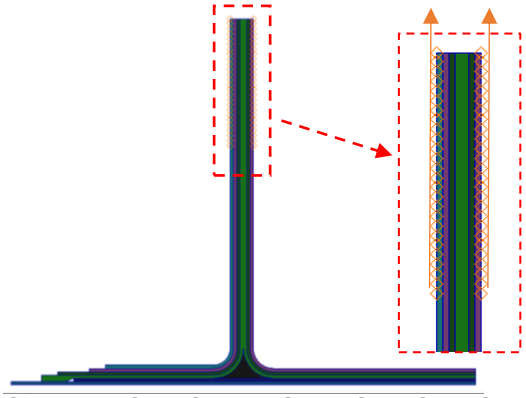

b) Tension boundary condition along the web.

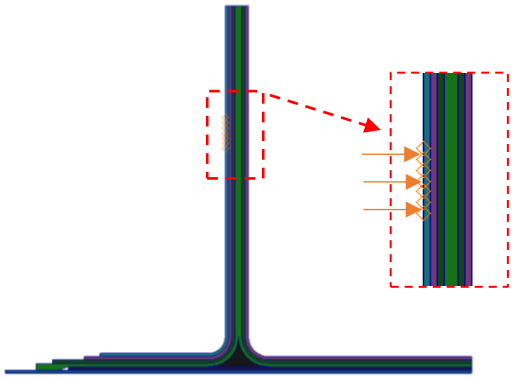

c) Bending boundary condition along the web.

Fig. 8 Analysis boundary conditions within the 3-D model.

The 2-D and 3-D models were both compared against test data and failed specimen images to determine the fidelity of the modeling efforts. Preliminary results are presented in the next section.

III. Finite Element Analysis Results

Finite element analyses were conducted using both the 2-D and 3-D models. The loading equivalent to test conditions was confirmed for each model using the summation of reaction forces at the nodes where clamp boundary conditions were applied. As previously mentioned, for the tension analyses, the approximate experimental failure corresponds to a displacement of 0.03 in. and an applied load of 2300 lb. just prior to initial failure. For the bending analyses, the approximate experimental failure load corresponds to a crosshead displacement of 0.1 in. and an applied load of 325 lb. just prior to initial failure. These values are consistent with the load and displacement data available in Refs. 5 and 6.

The non-stitched 2-D model was run using an Abaqus nonlinear static analysis, and the results of this analysis are compared to the digital image correlation (DIC) photogrammetric strain data for a stitched test article, as provided in Ref. 6, because no non-stitched articles were tested. This comparison between a non-stitched model and a stitched test article is a reasonable starting point because the test articles did not indicate that the failure initiated at the stitches, but rather that the stitches arrested the failure growth (delamination) that initiated away from the stitches. Strain

contour plots of the global x-direction (E_{11}) and y-direction (E_{22}) strains from the analysis of the tension load case of the 2-D model are compared to the corresponding test DIC strain contours in Figs. 9 and 10, respectively. The legend range for the analyses was aligned with the DIC legend shown in each figure for a visual comparison. Bending load case plots, plots for stitched models, and further discussion are located in Section IV.

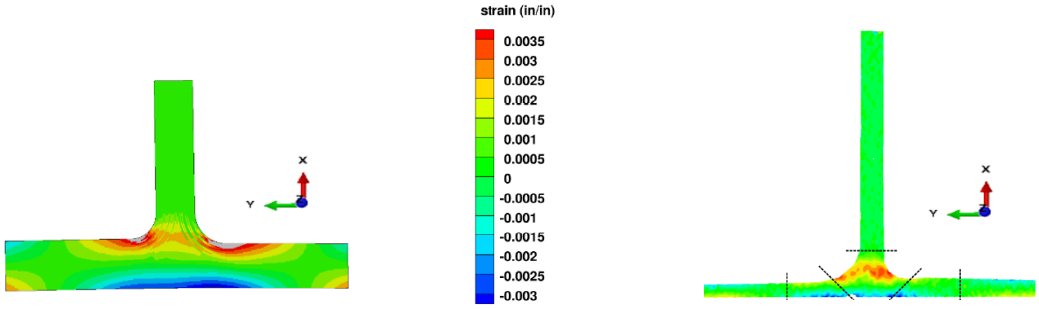

Fig. 9 E_{11} strain contours before initial failure in 2-D nonlinear model (left) and tension specimen DIC (right).

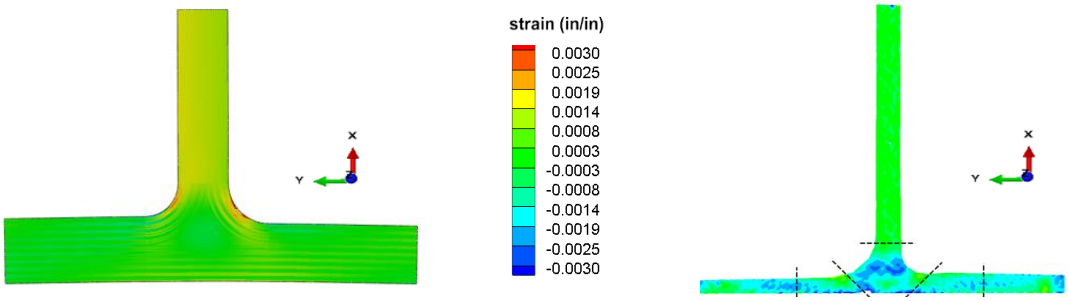

Fig. 10 E_{22} strain contours before initial failure in 2-D nonlinear model (left) and tension specimen DIC (right).

The non-stitched 3-D model was initially run with an Abaqus nonlinear static analysis and was also compared to the test specimen DIC provided in Ref. 6. The tension contour plots shown in Fig. 11 are comparisons of the global x-direction strain (E_{11}), while the transverse (global y-direction or E_{22}) strain comparisons are shown in Fig. 12. It is important to note that the nature of continuum shell elements makes the visual comparison complex since SC8R elements do not have a visual representation of the through-thickness direction, so the elements appear as flat plates or "slices" in the in-plane region. An example of a rotation of the model within Fig. 11a is shown in Fig. 11b, which shows these slices. Though it appears the elements are not "solid", there is indeed a full representation of the element-based results that can either be shown as an average over the entire stacking sequence, or the results can be shown at specific plies. Bending load case plots, plots for stitched models, and further 3-D discussion are located in Section IV.

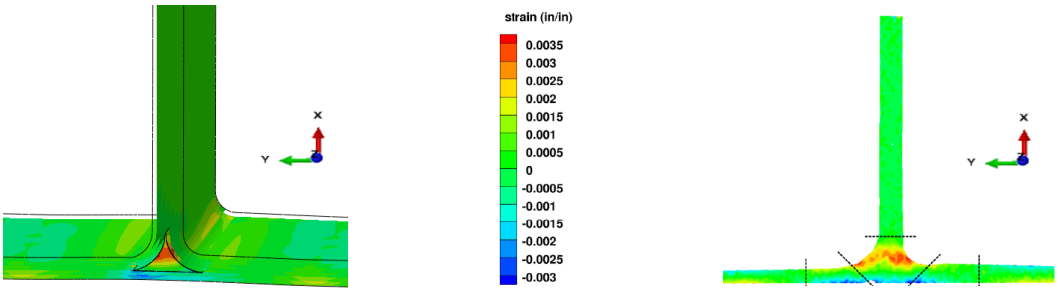

a) 3-D nonlinear model (left) and tension specimen DIC (right).

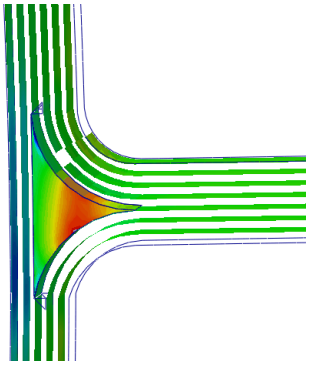

b) Rotated 3-D nonlinear model showing SC8R display issues.

Fig. 11 E_{11} contours before initial failure for tension loading comparison.

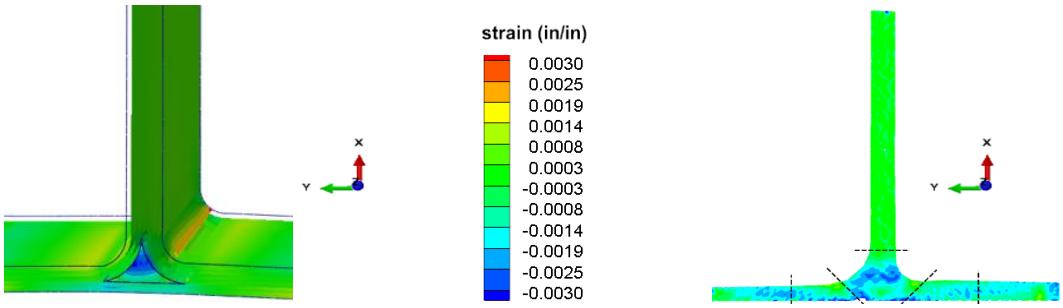

Fig. 12 E_{22} contours before initial failure in 3-D nonlinear model (left) and tension specimen DIC (right).

IV. Finite Element Model Results Discussion

As shown in Fig. 9, the 2-D cross-sectional model was able to capture elevated axial (E_{11} or global x-direction) strains at the radii of the specimen. Increased strain at the base of the web is visually apparent but appears to have a more significant positive to negative strain range than the test data. Positive strain peaks appear in the filleted region of the model, with a maximum strain of 0.0043 in/in in the grayed region, which is a 23% difference from the peak strain visually apparent in the test data. The results of the analysis predict a region of negative strain at the bottom skin ply, consistent with the test data. The transverse (E_{22} or global y-direction) strains shown in Fig. 10 indicate that there is greater predicted variation through the noodle area than the test specimen, though the trend of near-zero strain through the noodle and increased strain through the web is captured. Peaking again occurs at the fillet areas. For the E_{22} strains, however, the 2-D model underpredicts the expected minimum strain by 22%. These differences in strain for both E_{11} and E_{22} are limited to surface elements at the radius of the web, and the DIC system used to capture test data is unable to accurately calculate strain data at the extreme edges of test specimens. Due to this limitation, the 22% difference may be an “at worst” condition, with the true comparison closer than it appears.

The nonlinear 2-D static bending analysis of the non-stitched model was compared to a stitched test specimen under a bending load. For all bending specimens presented, the DIC camera was positioned toward the opposite face of the specimen from its position in the tension specimen testing. As such, the global y-direction is plotted in the opposite direction of that in the previous plots. The axial strain contours and test results are shown in Fig. 13, while the transverse contours and test results are shown in Fig. 14. The model captures an increased strain on the side of the web opposite the bending load, as seen in the test data in Fig. 13. The range of the strain appears higher in the model, but this may be attributed to the greater number of subdivisions in the scale range plotted. The maximum positive strain recorded in the E_{11} strain in the bending model is 0.003 in/in, matching the test data. The minimum strain is -0.0025 in/in, a 40% difference localized at two elements at the fillet radius. Likewise, this same phenomenon of greater positive to negative range for the transverse strains is shown in Fig. 14. For the E_{22} strain, the model predicts a peak strain of 0.006 in/in in a surface element at the fillet radius. The minimum strain is -0.0075 in/in, a 25% difference from the minimum strain observed in the test data. The model predicts greater strain in the web area than the test data in both the E_{11} and E_{22} strain contours, and this may be mitigated by using a PFA as opposed to the nonlinear static analysis presented here.

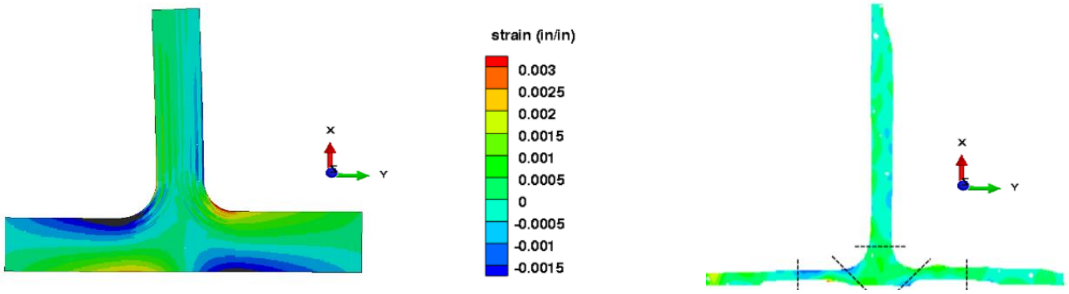

Fig. 13 E_{11} contours before initial failure in 2-D nonlinear model (left) and bending specimen DIC (right).

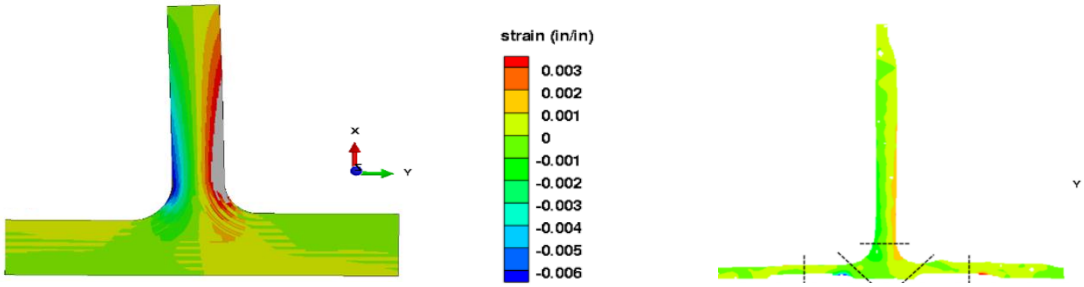

Fig. 14 E_{22} contours before initial failure in 2-D nonlinear model (left) and bending specimen DIC (right).

The stitched 2-D model was also run using an Abaqus nonlinear static analysis, and the strain results of this analysis are compared to the same strain DIC contours for the stitched test article as provided in Ref. 6. This comparison is shown in Fig. 15 through Fig. 18. The stitched models show similar maximum and minimum strains to the non-stitched models, exceeding the test data at the same elements.

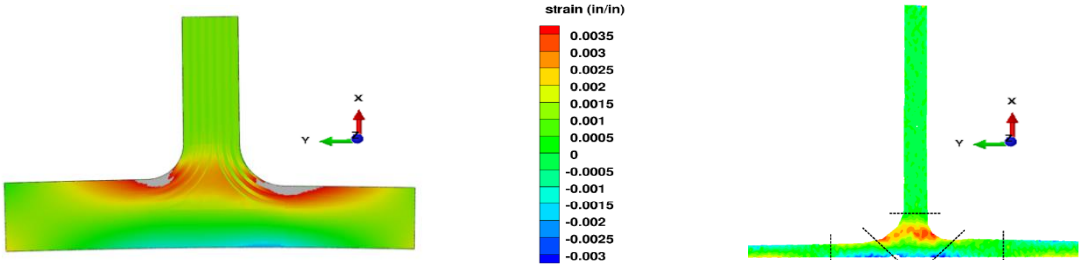

Fig. 15 E_{11} contours before initial failure in stitched 2-D nonlinear model (left) and the DIC tension specimen (right).

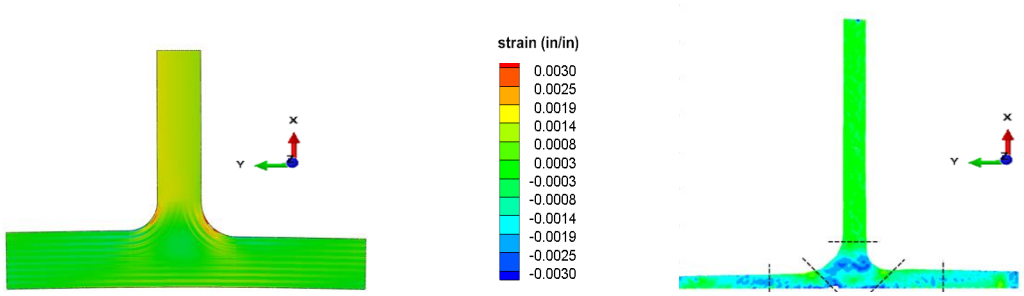

Fig. 16 E_{22} contours before initial failure in stitched 2-D nonlinear model (left) and DIC tension specimen (right).

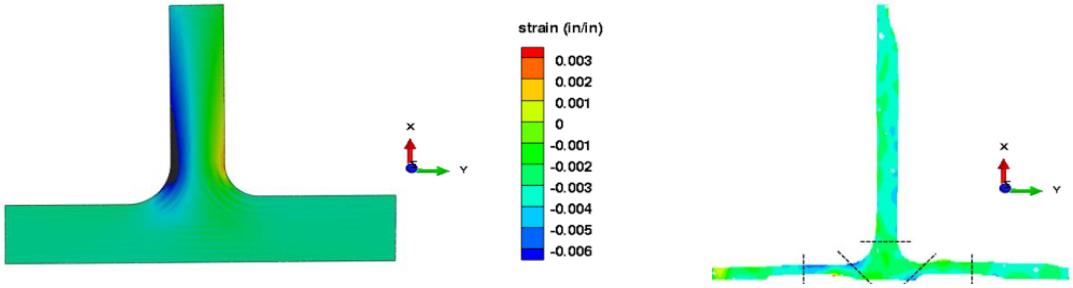

Fig. 17 E_{11} contours before initial failure in stitched 2-D nonlinear model (left) and DIC bending specimen (right).

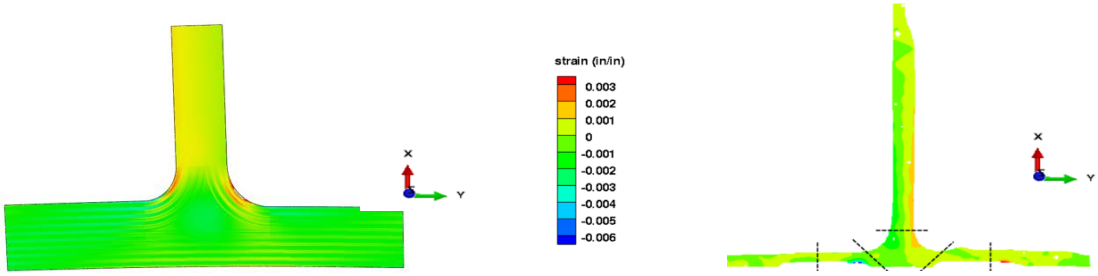

Fig. 18 E_{22} contours before initial failure in stitched 2-D nonlinear model (left) and DIC bending specimen (right).

Returning to the E_{11} comparisons for the 3-D model (Figs. 11 and 12 in the previous section), the model predicted elevated strains in the top of the noodle region, as well as through the plies in the corner regions. The model also predicted the area of negative strain along the bottom of the skin stack underneath the web. The model has a slightly larger predicted concentration of the increased positive strain than the test result, but this model does not contain stitches which may help stabilize some of the more severe strain concentrations. The C3D8 elements shown within the noodle region in all 3-D model images show results within any of the three dimensions and do not have the same display issues as the SC8R elements. The E_{22} contours within the analysis also visually appear to correspond well to the negative and positive strain locations shown in the DIC on the right of Fig. 12.

Nonlinear static bending analysis was also applied to the non-stitched model. The bending contour plots shown in Fig. 19 are comparisons of the x-direction strain, while the transverse strain comparisons are shown in Fig. 20. In the E_{11} comparisons, there is not a significant amount of contour variation, however the model was able to predict a visually similar contour plot when compared with the DIC of the bending specimen on the right, with the exception of a greater negative strain within the model in the area of the bending load. The E_{22} contours show more of a variation in contour color, and though the right side of the analysis corresponds well to the test data, the model seems to predict an additional area of increased strain on the side of the web opposite to the bending application.

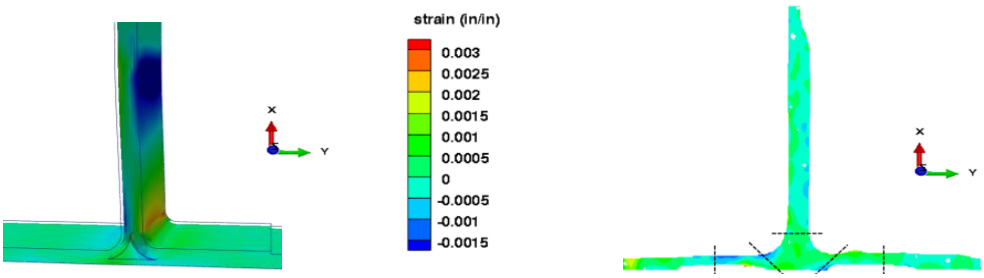

Fig. 19 E_{11} contours before initial failure in 3-D nonlinear model (left) and bending specimen DIC (right).

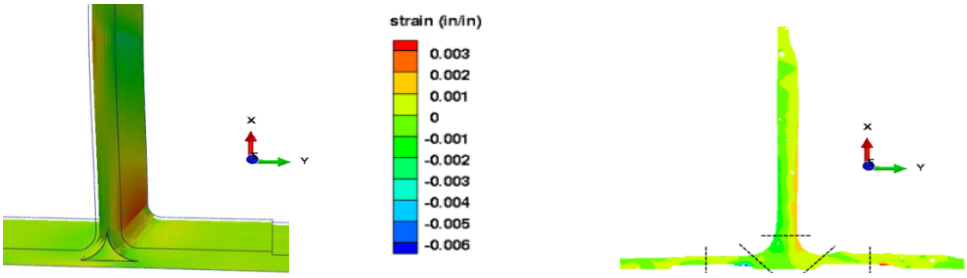

Fig. 20 E_{22} contours before initial failure in 3-D nonlinear model (left) and bending specimen DIC (right).

The stitched 3-D model was initially analyzed in Abaqus as a nonlinear static analysis, and eventually analyzed as a PFA. These PFA model results, prior to failure, were also compared to the test specimen DIC contours, as shown in Fig. 21 through Fig. 24. The tension-loaded E_{11} comparison shown in Fig. 21, indicates that the model was again able to predict elevated strains across the noodle region and the web plies around the radius. The addition of stitches within this model did help reduce some of the more severe strain concentrations seen in the non-stitched nonlinear analysis, however the reduction was likely not significant enough for the need for more complex models when observing pre-failure behavior. The E_{22} contours in Fig. 22 match much of the variation in positive and negative strains and are only missing the area of negative strain at the bottom of the skin directly under the noodle.

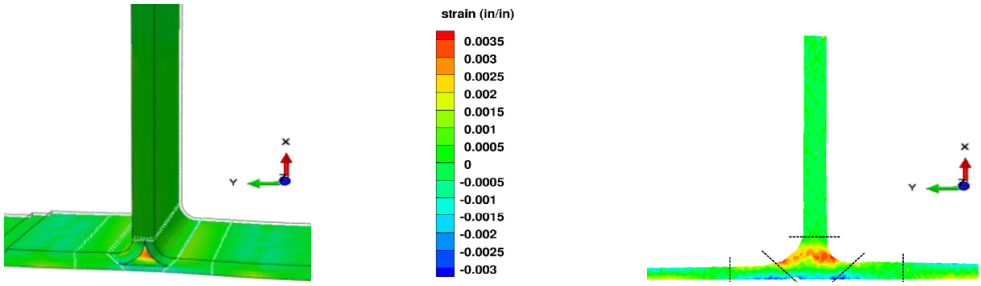

Fig. 21 E_{11} contours before initial failure in 3-D stitched PFA model (left) and tension specimen DIC (right).

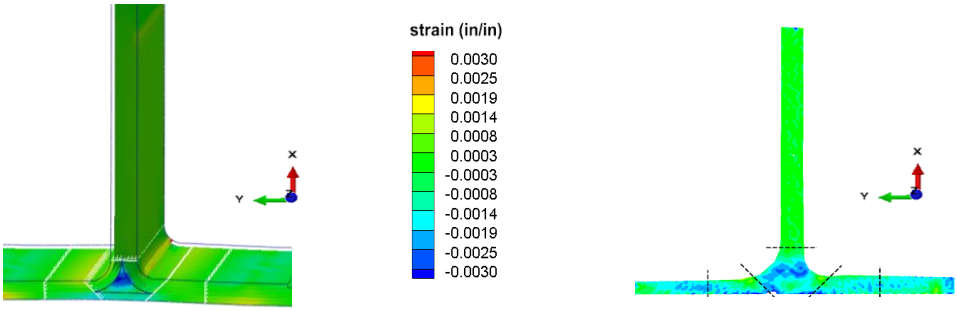

Fig. 22 E_{22} contours before initial failure in 3-D stitched PFA model (left) and tension specimen DIC (right).

The PFA for bending was also applied to the stitched model, as shown in the E_{11} comparison in Fig. 23 and the E_{22} comparison in Fig. 24. In the E_{11} comparisons, the model was able to predict a similar contour plot to the DIC of the bending specimen on the right, except for an additional area of positive strain on the right radius of the web. The E_{22} contours within the model show correlation with the increased strain on the side of the web where the bending was applied, but there is also again an extra strain concentration on the opposite (-y) side. A PFA with cohesive elements between plies may more accurately predict this advanced type of loading and strain response than the current model.

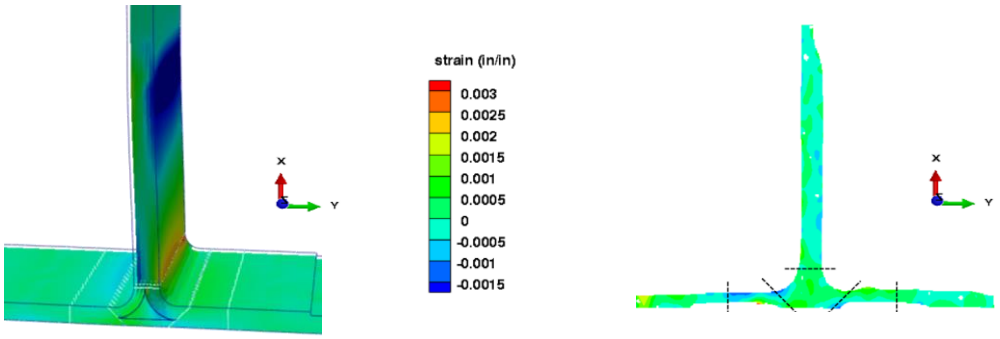

Fig. 23 E_{11} contours before initial failure in 3-D stitched PFA model (left) and bending specimen DIC (right).

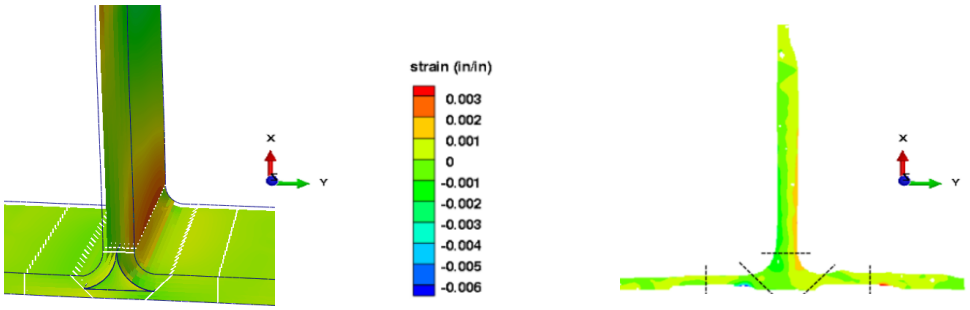

Fig. 24 E_{22} contours before initial failure in 3-D stitched PFA model (left) and bending specimen DIC (right).

The 2-D and 3-D comparisons between model predictions and test specimen data for non-stitched models with nonlinear analyses show agreement. The 3-D PFA model with stitches also shows agreement with both of the nonlinear analyses. Having correlation between the 2-D and 3-D models is promising for rapid creation of less complex models for investigative purposes, followed by full-fidelity models to verify the simplified model predictions. Additionally, T-cap specimen testing is planned during the HiCAM project to provide an opportunity to use the developed modeling approaches for predictive purposes, and to provide additional data for model validation and refinement.

V. Concluding Remarks

Stitched and resin infused composite structures are being investigated within the HiCAM project as one of the possible technologies to increase composite aircraft manufacturing rate. In order to carry out design and analysis, 2-D and 3-D models of previous tests conducted at LaRC were developed and investigated to establish analysis methods for stitched structures of this configuration. The 2-D and 3-D models developed in this preliminary study, and described herein, capture the strain patterns well when compared to observed DIC data for stitched T-cap specimens tested in either tension or bending loading. As anticipated, the 3-D model provided higher fidelity to the DIC data. This higher fidelity is attributed to the plane-strain assumption made to simplify the model to 2-D. While developed using T-cap test data, the developed methods are applicable to blade stiffeners used for many structures. While further refinement is possible via the inclusion of cohesive elements between plies, this may not be necessary to capture the desired level of detail for the analysis of structures under loading for which individual ply failure is of minor concern.

Analysis methods for the T-cap specimens is part of the analysis development work planned for stitched composites within the HiCAM project. Future work is expected to include additional DIC data for non-stitched and stitched T-cap specimens, that are currently under fabrication, to provide a more complete comparison between the

non-stitched finite element model analysis results and DIC data. Additional modeling development, including detailed PFA, should be also conducted for more complex test specimens (e.g., 7-point bend tests).

References

[1] Lovejoy, A. E., "PRSEUS Pressure Cube Test Data and Response," NASA/TM–2013-217795, May 2013.

[2] Yovanov, N., Lovejoy, A. E., Baraja, J., and Gould, K., "Design, Analysis and Testing of a PRSEUS Pressure Cube to Investigate Assembly Joints," 2012 Airworthiness & Sustainment Conference, Baltimore, MD, April 2-5, 2012.

[3] Jegley, D. C., Przekop, A., Lovejoy, A. E., Rouse, M. and Wu, T., "Structural Response of a Stitched Composite Hybrid Wing Body Center Section," AIAA Journal. Published Online:1 Dec. 2020, https://doi.org/10.2514/1.C035911.

[4] https://www.kuraray.us.com/products/fibers/vectran/

[5] Lovejoy, A. E., and Leone, F. A., Jr., "Tension and Bending Testing of an Integral T-cap for Stitched Composite Airframe Joints," AIAA 2016-2180, 57th AIAA/ASCE/AHS/ASC Structures, Structural Dynamics, and Materials Conference, San Diego, CA, January 4-8, 2016.

[6] Lovejoy, A. E., and Leone, F. A., Jr., "T-Cap Pull-Off and Bending Behavior for Stitched Structure," NASA/TM-2016-218971, April 2016.

[7] Velicki, A, Hoffman, K., Linton, K. A., Baraja, J., Wu, H-Y. T., and Thrash, P., "Hybrid Wing Body Multi-Bay Test Article Analysis and Assembly Final Report," NASA CR -2017-219668, September 2017.

[8] *Abaqus Analysis User's Guide 6.14*. Dassault Systèmes, 2014. Accessed on May 2, 2021. [Online] Available: http://130.149.89.49:2080/v6.14/books/usb/default.htm

[9] Damage Initiation for Fiber-Reinforced Composites, MIT Abaqus-docs, 2017. Accessed on May 2, 2021. [Online] Available: https://abaqus-docs.mit.edu/2017/English/SIMACAEMATRefMap/simamat-c-damageinitfibercomposite.htm

[10] Hexcel 8552 AS4 Unidirectional Prepreg 190 gsm & 35%RC Qualification Material Property Data Report, NCAMP CAM-RP-2010-002 Rev A, May 2011.